Simultaneous combined XRF-XRD analysis of geological sample: New methodological approach for on-site analysis on New-Caledonian Ni-rich harzburgite

Barbara Maestracci [a,b,*], Sylvain Delchini [b], Daniel Chateigner [a], Henry Pilliere [c], Luca Lutterotti [d], Evgeny Borovin [d]

[a] 6 boulevard Maréchal Juin, CRISMAT Laboratory, University of Caen-Normandie, Caen, France
[b] Bureau de Recherche Géologique et Minière (BRGM), Orléans, France
[c] Inel Innov, Jargeau, France
[d] Department of Materials Engineering and Industrial Technologies, University of Trento, Trento, Italy

ARTICLE INFO

ABSTRACT

There is a growing interest in on-site, real-time analytical solutions for mining and environmental projects to characterize large areas and/or volumes of raw materials that are sometimes highly heterogeneous in terms of elemental distribution and mineralogy. Several fast and cost-effective methods are used for rapid on-site screening and real-time chemical and mineralogical characterization, such as portable X-ray fluorescence (pXRF) and X-ray diffraction (pXRD). However, these methods are not always applicable due to limitations in the detection and quantification of light elements (Mg, Al, Si) for pXRF or complex or minor minerals for pXRD, whose results need to be supported by laboratory analysis.

This study presents a new methodological approach for in situ rapid chemical and mineralogical characterization of samples, based on the use of a transportable instrument (called ID2B) that allows, in a single acquisition step, a combined XRD-XRF analysis to identify and quantify the chemical elements and their associated minerals. The HI0 harzburgite sample from New Caledonia used to evaluate the data was analyzed in the laboratory (SEM-EDS, EPMA, XRF and XRD) and with the ID2B instrument to highlight the potential of our new methodology. In order to demonstrate the interest of using the ID2B combined XRF-XRD analysis approach directly in the field, where sample preparation is not always easy to implement, this comparison was made on the same sample (HI0), prepared in two different ways, either as a powderized (optimal preparation) or as-sawn (unprepared) sample. After automated processing of the combined XRF-XRD datasets acquired with the ID2B instrument, the chemical elements and mineralogical phases identified on both the powder and as-sawn samples are identical to the laboratory analyses.

The chemical proportions calculated from the combined XRF-XRD data sets are also close to the laboratory XRF analysis with relative errors <5 % for Al, Mg and Si and even closer for Ca, Cr, Mn, Ni and Fe. The variability in the calculated chemical proportions is attributed to the sample heterogeneity highlighted by the mineral proportions that vary slightly between the laboratory XRD and XRD ID2B analyses of the powder, and more pronounced for the as-sawn XRD ID2B analysis. These observations show that the combined XRF-XRD approach performed on powder and as-sawn samples provides accurate chemical and mineralogical results to those obtained in the laboratory. The deployment of this new methodological approach directly on the field can provide valuable chemical and mineralogical analyses.

1. Introduction

The scientific community is facing a heavy demand from industrials and especially the raw-material and environmental communities for on-site real-time analyses which can provide decision-making support for field exploration, sorting and quality control of materials, or the

---

monitoring of processes (Mauger, 2007; Siddiqui et al., 2017). Traditionally laboratory instruments were developed to achieve raw-materials characterizations, providing the most reliable geochemical and mineralogical data. However, such instruments are usually not adapted to respond in real-time to the industrial needs, hampered by long samples shipping and preparation, long analyses and data processing, use of many consumables, resulting in time-consuming and expensive methodologies. To overcome these problems analytical technologies designed for the laboratory have been adapted for on-site use and portable field instruments have emerged. For instance portable X-Ray Fluorescence (pXRF) has been developed for >20 years and is now used in a wide range of applications in archaeology, environmental sciences, soil analysis and agriculture, raw material exploration and sorting (Lemière, 2018; Lemière and Uvarova, 2020). More recently, the miniaturization of analytical components (e.g. X-ray tubes, detectors and processors), combined with the improvement of software packages, makes X-Ray Diffraction (XRD) a credible analytical technique that can be deployed in the field (Sarrazin et al., 2005). Several studies showed the valuable contribution of portable XRD (pXRD) especially for mineral exploration, for which identification and quantification of mineral assemblages is valuable information (Burkett et al., 2015; Sarala and Koskinen, 2018). Uvarova et al. (2016, 2020) showed that coupling pXRF and pXRD instruments on field provides cost-effective, rapid, repeatable and accurate determination of sample's geochemistry and mineralogy, which in turn allows discrimination of lithologies and ore types and helps to identify penalizing or valuable chemical elements and/or minerals. However, the use of pXRF and pXRD, either individually or coupled, is not possible in all contexts due to limitations in technical capabilities such as the detection and quantification of (1) light elements up to Mg, Al, Si or even Mg for pXRF (Lemière and Uvarova, 2020), or of (2) complex or minor minerals for pXRD (Sarala and Koskinen, 2018), and whose results have to be supported by laboratory analyses.

Recently, the development of transportable on-site instruments allowing to perform a combined approach to merge both XRD and XRF data acquisition and analysis, offer fast and precise new analytical perspectives to obtain chemical and mineralogical information (Bortolotti et al., 2017). These two analytical techniques are very complementary. On the one hand XRD allows the identification and quantification of minerals even made of light elements, but is less sensitive to (i) chemical substitutions of *Z*-close elements and (ii) poorly crystallized/amorphous phases. On the other hand, XRF allows the identification of elements whatever the crystallized state but does not provide information on the long-range order of the minerals, i.e. cannot distinguish isocompositional phases stabilized as different space groups, and does not easily detect small-Z elements. Coupling these two techniques in a single acquisition step therefore provides the missing link between elemental and phase analyses. A customized analytical X-ray instrumentation (called ID2B) has then been developed within the frame of the SOLSA project (H2020 SOLSA: G.A. No. 689868) to perform fast (< 30 min) and combined X-ray data acquisition on-site in order to in-situ collect, quasi-simultaneously diffracted and fluorescent X-ray signatures from the same sample volume. This instrumental configuration is accompanied by the use of a modular sample holder capable of accommodating samples of different shapes, thus allowing the combined XRF-XRD analysis to be carried out both on prepared samples (e.g. powders) and on samples with little or no preparation (e.g. saw cuts, rocks), provided that the surface to be analyzed is flat enough.

In order to assess data and analyses consistency between laboratory and the on-site ID2B instruments, a natural sample called HI0 corresponding to a Ni-rich serpentinized harzburgite from New-Caledonia has been analyzed. Elemental and mineralogical results obtained from laboratory instruments (SEM-EDS, EPMA, XRF and XRD) have been compared to those calculated with the ID2B instrument from the XRF-XRD combined analysis. In addition, in order to demonstrate the interest of using the combined XRF-XRD analysis approach directly in the

field, where sample preparation is not always easy to carry out, this comparison has been made on the same sample (HI0) but prepared in different ways. The first preparation corresponds to a powder that requires a high degree of preparation with successive crushing and grinding steps that are not easy to implement in the field, while the second preparation is an as-sawn sample that requires little preparation but whose analysis is subject to matrix and preferred orientation effects.

2. Materials and methods

2.1. Sample

The studied serpentinized harzburgite sample HI0 (Fig. 1) studied was provided by SLN (Société Le Nickel, ERAMET, Népoui, New Caledonia). In New-Caledonia, Eramet-SLN defined the typology of nickel laterite in relationship with the degree of serpentinization and weathering of the ultramafic bedrock that is correlated with enrichment in Ni (Orloff, 1968; Trotet et al., 2015). According to the nomenclature used by the SLN, the sample HI0 corresponds to a harzburgite ("H" symbol) with a strong Ni-enrichment potential as shown by the degree of serpentinization in the intermediate facies ("I" symbol) (between 15 and 45 % of serpentine) and not affected by meteoric alteration ("0" symbol). A macroscopic observation of the raw drilled core sample (Fig. 1a) shows a massive, dense and smooth rock characterized by a greenish matrix composed of olivine integrating millimetric to centimetric sub-rounded grey grains of pyroxene.

The overall sample is cross-cut by several typically 1 mm-wide black veins (Fig. 1b), without noticeable preferred direction and filled of leaf minerals which would appear to be minerals of the serpentine family. Not distinguishable on a drill core surface, but well identified on a fresh break or sawn cross-sections, multiple small black grains identified as chromite are observed.

2.2. Sample preparation

In order to evaluate the data consistency between laboratory and ID2B analyses we tested our method on three different sample preparations: a polished section, a drill core fragment (Fig. 1a) and a powder sample. The thin section was performed for polarized light microscopy, scanning electron microscopy and EPMA. The drill core fragment was analyzed only on the combined XRD-XRF ID2B instrument. And the powder was analyzed by XRD and XRF in the laboratory and on the combined XRD-XRF ID2B instrument.

2.3. Laboratory analytical methods

Polarized light (PLM, LEICA with a x50 objective) and Scanning Electron (SEM-EDS; Tescan Mira3 XMU) Microscopies were used to get the mineralogy and the rock geological textures. SEM coupled with energy dispersive spectrometer (EDAX TEAM EDS system with an Apollo XPP silicon drift detector) at operating conditions of 15 kV and 5 nA were applied for semi-quantitative in-situ chemical analysis (analyses time of 50 s/point) and elemental mapping (Figs. 3c and 3d).

2.4. Electron probe micro-analysis (EPMA)

Elemental characterization of each of the mineral phases, on thin section, was completed with quantitative electron probe microanalyses (EPMA) performed with a CAMECA SX-FIVE electron microprobe equipped with five vertical Wavelength Dispersive Spectrometers (WDS). The measurement conditions were made with an accelerating voltage of 15 kV, a current of 20 nA and a spot size of 1–2 μm. In order to obtain quantifications, the machine was calibrated with periclase for Mg (K_α), albite for Na (K_α), orthoclase for K (K_α), andradite for Si and Ca (K_α), corundum for Al (K_α), chromite for Cr (K_α), hematite for Fe (K_α), $MnTiO_3$ for Mn and Ti (K_α) and NiO for Ni (K_α). Matrix corrections were

Fig. 1. Macroscopic photographs of the HI0 serpentinized harzburgite. (a) Drill core showing olivine matrix, serpentine veins network, enstatite serpentinized and enstatite, and (b) as-sawn sample of the drilled core showing iron oxide, chromite, olivine matrix and serpentine veins network.

performed with the PAP computing programs of Pouchou and Pichoir (1984). For each sample, the chemical composition was obtained from about ten measurements on average (varying from 6 to 16 measurements depending on the mineral).

2.5. X-ray fluorescence (XRF) and X-ray diffraction (XRD)

Bulk chemical and mineralogical laboratory analyses have been performed on powder sample using X-ray fluorescence (XRF) for major elements and X-ray diffraction (XRD) for minerals Quantitative Phase Analysis (QPA). For XRF analysis, after calcination at 1025 °C of the powder and addition of lithium tetraborate ($Li_2B_4O_7$) a glass bead was prepared (Keith & Keith and Hutton, 1969; Kimura and Yamada, 1996; Sugisaki et al., 1981) and analyzed with a Zetium Panalytical spectrometer at BRGM (Orléans-France), equipped with a rhodium tube and a Xenon detector.

XRD data were acquired using a Xpert Panalytical MPD diffractometer (θ-θ Bragg-Brentano mode) using a Co K_α ($K_{\alpha 1}$ = 1.78900 Å and $K_{\alpha 2}$ = 1.79289 Å) averaged radiation and a XCelerator detector at CRISMAT (Caen-France). Data were collected at room temperature from 5° to 140° in 2θ range, for 8 h using a scan step of 0.0167° and spinning at 4 rps. Instrumental contributions of diffraction instruments in the patterns were determined using the LaB6 660c standard powder from NIST (NIST, 2015). Mineral identification was performed using the Crystallography Open Database (COD) (Gražulis et al., 2012) and the Inorganic Crystal Structure Database (ICSD) (Hellenbrandt, 2004; Belsky et al., 2002). QPA was operated using Rietveld refinement as implemented in the MAUD software (Lutterotti et al., 1999).

2.6. SOLSA ID2B combined instruments

XRF-XRD combined measurements on powder and as-sawn raw samples were performed by the on-site transportable SOLSA ID2B combined instruments (Fig. 2) allowing quasi-simultaneous measurement of XRF and XRD signals at room temperature. X-ray fluorescence spectra were acquired using a Mo micro-source radiation and an Amptek X-123SDD Silicon Drift Detector placed nearly vertically at 2 mm over the sample to ensure measurement of the lighter elements down to Z = 12 (Mg). Data were collected for a quantitative XRF model from 0.1 to 15 keV. X-ray powder diffraction data were acquired in asymmetric mode using Co K_α average radiation ($K_{\alpha 1}$ = 1.78900 Å and $K_{\alpha 2}$ = 1.79289 Å) and equipped with a INEL curved position sensitive detector which spans the whole $5 \le 2\theta \le 120°$ range simultaneously. For this diffractometer, the instrumental function has also been defined using the LaB6 660c standard powder from NIST, and the databases and software are the same as for the laboratory instrument part.

Traditionally, the chemical and mineralogical sample characterizations are carried out using separate XRF and XRD instruments. The data obtained are processed independently, as is done in this study for XRF and XRD laboratory analyses. However, several studies have shown that combined XRF-XRD analysis is a powerful tool for material characterization (Lutterotti et al., 2019; Bortolotti et al., 2017; Secchi et al., 2018). The procedure for simultaneous fitting of XRD and XRF data is as follow.

QPA from the XRD data is first performed using the Full Profile Search Match (FPSM) software procedure (Lutterotti et al., 2019) implemented in MAUD software, which automatedly identifies and
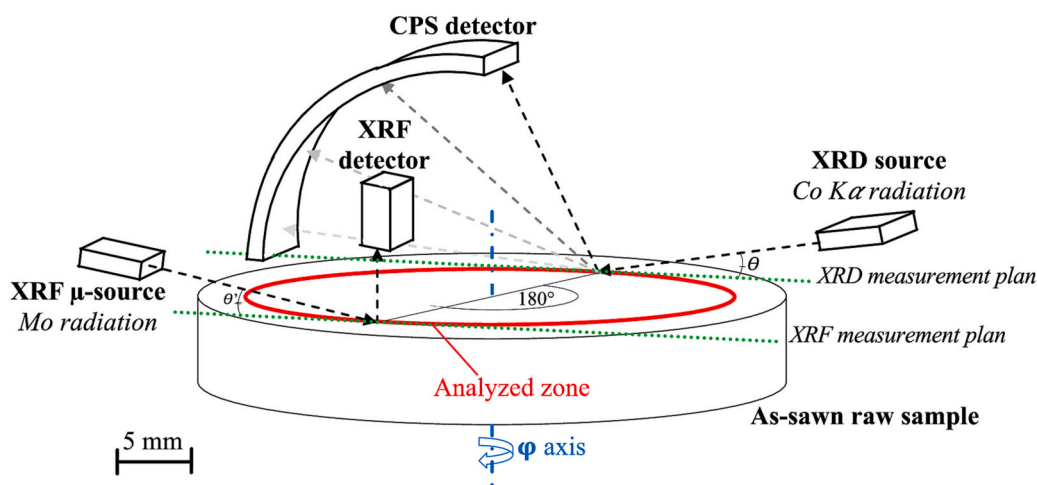
Fig. 2. SOLSA ID2B combined instrument scheme showing x-ray sources and detectors. A continuous φ rotation was imposed to the sample during measurements. The red line represents the area analyzed by the two techniques (XRF and XRD) when the sample is rotated completely on the φ axis. The green dotted lines represent the measurement planes of the two techniques used. The dotted black and grey lines represent the path taken by the beams. The XRD and XRF analysis points are 180° apart. The measurement planes of the two techniques are parallel to each other. The θ angle is the angle between the XRD sample plane and the XRD incident beam. The θ' angle is the angle between the sample plane and the XRF incident beam. (For interpretation of the references to color in this figure legend, the reader is referred to the web version of this article.)

quantifies diffracting phases present in the sample. The database used for this mineral search step is the Crystallography Open Database (COD) (Gražulis et al., 2009; Gražulis et al., 2012; Vaitkus et al., 2021). From the identified minerals, a first list of elements is established to deserve XRF pattern fit, this former list being completed with other elements detected in the XRF and EDX spectra and not evidenced in XRD.

For both XRD and XRF pattern fits, all beam paths through the sample and instrumental configurations (incident and outgoing beam paths, including air and windows, etc.) are taken into account and calibrated, including elastic scattering and photoelectric absorption/fluorescence scattering.

XRD data are modelled using the Rietveld method, i.e. including structural, microstructural and phase quantity determinations, while for XRF data the Le Boër model is used to determine elemental quantities. Elemental substitutions within crystal structures are also taken into account. Since sample definition is included within the Rietveld fit, the so-called matrix effects usually occurring for XRF analyses are taken into account at once during a Combined Analysis of all the datasets. This analysis uses the minimization of the following weighted cost function:

$$W = \sum_{t=1}^{T} u_t \sum_{i=1}^{I} w_{it} \left(y_{it}^{calc} - y_{it}^{meas} \right)^2$$

In which T is the total number of patterns (XRD and XRF), I is the total number of measured points, of intensity y_{it}^{meas} in each pattern, y_{it}^{calc} the modelled intensity for the i^{st} point of the tth pattern, w_{it} the statistical weight associated to each point i of pattern t (chosen as $1/\sqrt{y_{it}^{meas}}$) and u_t

a weight associated to each pattern. The choice of u_t is fixed during the combined refinement to the weighted pattern reliability factors R_{wp} (Hill and Howard, 1987). The W function taking simulated and observed XRD and XRF data are fitted to the measured XRD and XRF values using a Marquardt least squares algorithm, finally ending to a global fit solution satisfying both elemental and phase quantification of the analyzed sample.

3. Results and discussion

3.1. Mineral morphological and geological texture characterization (optical microscopy and SEM) and mineral chemistry (EPMA)

Optical microscopy (Fig. 3a and 3b) and SEM (Fig. 3c and 3d) observations show a more or less dense and penetrating network of anastomosed micrometric to millimetric serpentine veins, formed at the expense of the olivine whose initial form is generally preserved (Figs. 3a and 3b). In some areas, the olivine only remains in the form of small ovoids separated from each other by the serpentine veins. The three other identified minerals are millimetric orthopyroxene (enstatite) and chromite and few micrometric clinopyroxene (diopside). These minerals are well preserved and weakly fractured by serpentine veins. This mineral texture is typical of the first markers of serpentinization processes in which mainly the olivine is fractured and replaced by serpentine (Orloff, 1968; Trotet et al., 2015; Wicks and Whittaker, 1977).

The average elemental compositions of the minerals measured by
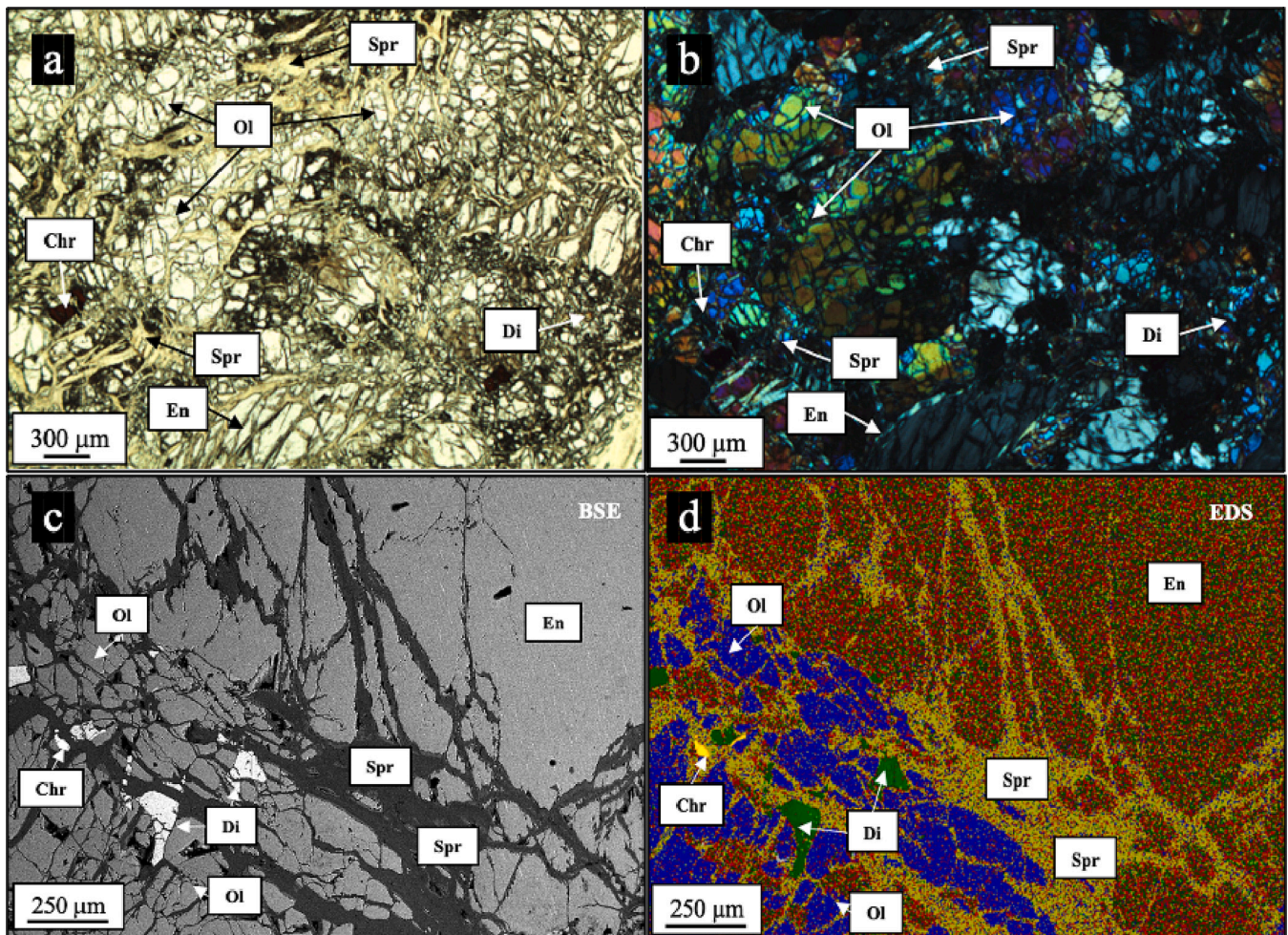
Fig. 3. Optical microscopy photographs of the HI0 sample under (a) plane-polarized and (b) crossed-polars; (c) back reflection SEM image and (d) SEM-EDX elemental mapping (mineral abbreviations: Spr: Serpentine; Ol: Olivine; En: Enstatite; Di: Diopside; Chr: Chromite).

EPMA in sample HI0 with the corresponding calculated structural formula are given in Table 1. Both olivine and orthopyroxene have a Mg-rich composition (the Mg/Fe substitution rate is about 86 % for both). Si, Mg and Fe are accompanied in lower proportion by NiO (0.40 wt%) and MnO (0.11 wt%) for the forsterite, and by Al_2O_3 (2.11 wt%), CaO (1.20 wt%), Cr_2O_3 (0.68 wt%), MnO (0.13 wt%) and NiO (0.1 wt%) for enstatite. The average calculated structural formulae of forsterite (($Mg_{1.82}Fe_{0.17}$ $Ni_{0.01}$)SiO_4) and enstatite (($Mg_{1.75}Ca_{0.04}Cr_{0.02}Fe_{0.15}$) ($Si_{1.95}Al_{0.09}$)$O_6$) are similar to those reported for samples from New-Caledonia (Ulrich et al., 2019; Muñoz et al., 2019).

Two types of serpentine called lizardite-2H1 and lizardite-1T were characterized by EPMA with similar compositions for major elements (40 wt% of SiO_2, between 33 and 36 wt% of MgO, and 5 wt% of FeO). On the other hand, variations in the minor elements are observable. Lizardite-2H1 is richer in Cr_2O_3 (0.37 wt%) and depleted in NiO (0.09 wt%) while the lizardite-1T is enriched in NiO (0.45 wt%) and depleted in Cr_2O_3 (0.01 wt%).

The average structural formulae of lizardite-2H1 ($Mg_{2.68}$ $Fe_{0.24}Cr_{0.02}$)($Si_{1.99}$ $Al_{0.05}$)$O_5(OH)_4$) and lizardite-1T (($Mg_{2.53}$ $Fe_{0.23}$ $Ni_{0.02}$)($Si_{2.07}$ $Al_{0.05}$)$O_5(OH)_4$) show that the number of tetrahedral cations is slightly in excess (2.04 and 2.12 instead of 2) compared to the ideal formula of serpentine ($Mg_3Si_2O_5(OH)_4$). In contrast, the number of cations in octahedral sites is slightly deficient (2.94 and 2.78). These results are similar to those reported for samples from New Caledonia (Manceau et al., 1985; Maubec et al., 2021).

Measured composition for chromites show high chromium, aluminium, iron and magnesium content (38.2 wt% Cr_2O_3, 31.3 wt% Al_2O_3, 16.3 wt% FeO, 13.8 wt% MgO). A low content of manganese (0.20 wt% MnO) has been measured as well as very low proportions of Ni, Si and Ca (< 0.1 wt%). The composition of HI0 chromite is similar to that reported for other samples in New-Caledonia (Ulrich et al., 2010; Wells et al., 2022).

3.2. Bulk chemical composition of HI0 using XRF

XRF analysis from reference laboratory measurements (Table 2) shows that HI0 is essentially composed of SiO_2 (44.07 wt%), MgO (46.68 wt%) and FeO (7.82 wt%) oxides. These elements belong to the major minerals (Fig. 3) identified in HI0 (forsterite, enstatite and serpentine) and are accompanied by low contents in NiO (0.34 wt%),

Table 2

Bulk chemical (wt%) recalculated composition of HI0 sample obtained from XRF measurements on pearls (laboratory instrument), powder and as-sawn samples (field instrument) major elements. Oxides compositions are only calculation given from elemental composition and not corresponding to oxide phases present in the sample as is.

Major element (wt%)	XRF Laboratory *Pearl*	XRF ID2B *Powder*	XRF ID2B *As-sawn sample*
Al_2O_3	0.53	0.44	0.51
CaO	0.39	0.58	0.74
Cr_2O_3	0.45	0.38	0.59
FeO	7.82	12.84	9.66
MgO	46.68	39.69	41.27
MnO	0.12	0.19	0.24
NiO	0.34	0.59	0.36
SiO_2	44.07	43.73	45.55
SUM	100	100	100

Cr_2O_3 (0.45 wt%), Al_2O_3 (0.53 wt%), MnO (0.12 wt%) and CaO (0.39 wt%). As showed by EPMA analyses on minerals composing HI0, serpentines (lizardite-2H1 and lizardite-1T) and forsterite are the main NiO-bearing minerals and chromite and enstatite are the main Cr_2O_3 and Al_2O_3-bearing minerals (Table 1). CaO is mainly related to the presence of diopside (not analyzed) and enstatite to a lesser amount, while MnO is present in very low proportion in all the minerals (Table 1).

The combined ID2B results on powder and as-sawn raw samples also mainly indicate that HI0 is composed of Si, Mg and Fe (Table 2). The SiO_2 (43.73 and 45.55 wt% for the powder and as-sawn raw samples respectively) and MgO (39.69 and 41.27 wt%) content values are similar to the ones obtained with the laboratory instrument (39.9 wt% SiO_2 and 41.9 wt% MgO). However, the FeO contents measured with the ID2B on the powder (12.84 wt%) and on the as-sawn sample (9.66 wt%) seem to be overestimated compared to the FeO content obtained in the laboratory. The first factor that could explain this overestimation concerns the heterogeneity of the sample when measured on an as-sawn sample. Indeed, in the presence of zones with a high concentration of Fe, such as veins rich in iron, nugget effects can lead to an overestimation of the iron content. The second explanation is related to the geometry of the ID2B instrument where the distance between the XRF detector and the sample surface influences the detection limits of the lighter elements. In other

Table 1

Average chemical composition and structural formulae of the minerals identified in HI0 sample measured by EPMA (Av.: average; σ: standard deviation; Tetra.: tetrahedral site; oct.: octahedra site). Oxydes compositions are only calculation given from elemental composition and not corresponding to oxide phases present in the sample as is.

	Olivine		Enstatite		Lizardite-2H1		Lizardite-1T		Chromite	
Number of analyses	*10*		*12*		*6*		*9*		*16*	
w%	Av.	σ	Av.	σ	Av.	σ	Av.	σ	Av.	σ
Al_2O_3	0.00	0.00	2.11	0.14	0.87	0.40	0.80	0.50	31.26	3.46
SiO_2	41.26	0.31	56.67	0.44	40.05	1.70	40.91	1.40	0.03	0.04
MgO	50.49	0.21	34.11	0.43	36.24	1.29	33.55	1.65	13.81	0.60
CaO	0.01	0.01	1.20	0.58	0.02	0.02	0.03	0.01	0.01	0.01
NiO	0.40	0.03	0.10	0.01	0.09	0.02	0.45	0.05	0.08	0.02
MnO	0.11	0.02	0.13	0.01	0.10	0.01	0.10	0.04	0.20	0.03
Cr_2O_3	0.01	0.01	0.68	0.08	0.37	0.19	0.01	0.01	38.19	4.30
FeO	8.16	0.35	5.32	0.22	5.78	0.90	5.37	1.04	16.04	0.88
Total	**100.44**		**100.32**		**83.52**		**81.21**		**99.61**	
n Oxygen	*4.00*		*6.00*		*7.00*		*7.00*		*32.00*	
Al^{3+}	0.00	0.00	0.09	0.01	0.05	0.02	0.05	0.03	8.73	0.87
Si^{4+}	1.00	0.00	1.95	0.01	1.99	0.08	2.07	0.06	0.01	0.01
Σ tetra.	1.00		2.03		2.04		2.12		1.09	
Mg^{2+}	1.82	0.01	1.75	0.01	2.68	0.10	2.53	0.10	4.88	0.16
Ca^{2+}	0.00	0.00	0.04	0.02	0.00	0.00	0.00	0.00	0.00	0.00
Ni^{2+}	0.01	0.00	0.00	0.00	0.00	0.00	0.02	0.00	0.01	0.00
Mn^{2+}	0.00	0.00	0.00	0.00	0.00	0.00	0.00	0.00	0.04	0.01
Cr^{3+}	0.00	0.00	0.02	0.00	0.01	0.01	0.00	0.00	7.17	0.87
Fe^{2+}	0.17	0.01	0.15	0.01	0.24	0.04	0.23	0.04	3.19	0.20
Σ oct.	2.00		1.97		2.94		2.78		1.91	

words, when the XRF detector is too far from the sample surface, the magnesium concentration can be underestimated from 46.68 wt% to 39.69 wt% on powder sample. The algorithm used by MAUD software then compensates for the magnesium loss by overestimating the iron concentration. Finally, the third explanation concerns the presence of crystallographic texture within the sample. The latter influences the intensity of certain diffraction peaks similarly, as do certain substitutions, such as the Fe—Mg substitution present in olivine. It is therefore impossible in the current state of the algorithm to deconvolute the intensity of the peak by detailing precisely the contribution due to the Fe—Mg substitution from that due to the crystallographic texture. Low-content elements from laboratory measurements (NiO, Cr_2O_3, Al_2O_3, MnO and CaO) have also been identified using the ID2B instrument on powder and as-sawn samples, with proportions in the same order of magnitude as from XRF laboratory analysis (< 1 wt%).

3.3. Composition and QPA using XRD

Regardless of the used diffractometer, X-ray diffraction analyses reveal the same crystalline minerals: serpentines (lizardite-1T and 2H1), olivine, chromite and enstatite (Table 3). All of the detected minerals could be subjected to elemental variations, e.g. by substitution (Table 3), and the structural formulas of the actual minerals in the samples might deviate slightly from these identified in the Table 3 as illustrated by the EPMA chemical compositions measured (Table 1). In such a case, independent information is usually required for crossed-checking of XRD analyses using for instance bulk or in-situ chemical analyses (EDX-SEM, ICP-AES) in order to attest global or local element compositions and/or stoichiometries. Using a combined fit for XRD and XRF on the contrary (ID2B instrument) allows the information on these substitutions by a single analysis on both powder and as-sawn raw sample.

The mineral quantification results obtained on the powder sample (Table 4 and Fig. 4) after combined Rietveld and XRF refinements using the ID2B treatment procedure are in agreement with the laboratory results also measured on powder. With regard to possible elemental substitutions, olivine and enstatite are ternary Fe-Mg-Ni and Ca-Mg-Mn solid solutions respectively. For olivine, due to the similarity of the electronic effect of the Ni—Fe cations, it is hardly possible to resolve their mutual occupation. According to the literature and microprobe analysis, Ni in New Caledonia can substitute to Fe and Mg in olivine, and

to Mg in lizardite-1T. With this knowledge, Ni was incorporated into the octahedral cationic sites for olivine and lizardite-1T, the Ni-bearing minerals present in HI0 during the Rietveld refinement. However, after refinement, only lizardite-1T show a percentage of Ni present in the octahedral sites (2 ± 1 wt% for ID2B powder, Table 4). These results are justified by the strong difference in electronic effect between Mg and Ni in olivine.

As illustrated in the Fig. 5 by the modelled theorical diffractograms of different solid solutions of olivine, this difference in the electronic effect induces a change in the relative intensity of the peaks in a diffractogram as a function of the substitution ratio (Fig. 5). This difference is similar to that observed for Mg—Fe substitution. However, according to the EPMA results and the literature, olivine should be the main Ni-bearing minerals. In these minerals, the substitution would be a replacement of Fe by Ni. However, the electronic and steric effects of Ni and Fe cations being very close, it is hardly possible to resolve their mutual occupation and to observe a difference in the diffractograms, and as a result refinement only favor the presence of Fe in the olivine at the expense of Ni for these two minerals (Fig. 5). Thus, although the refinement of substitutions is possible with the XRF-XRD, the cross-referencing with bibliographic and/or laboratory data allows a more critical and global view of the results obtained on the XRF-XRD.

A substitution of Mg by Ni on lizardite-1T was also characterized using Raman analysis according to El Mendili et al. (2019) in similar samples. Only the XRF-XRD allows to refine this substitution by Rietveld refinement. Concerning the mineral quantification of the HI0 sample, serpentines represent at least 40 wt% of the minerals. Regardless of the instrument, on the powder sample, olivine and enstatite represent respectively 42 wt% and 15 wt%, while on the as-sawn sample, the weight % are reversed. Finally, the only mineral detected in lower amount, chromite, is refined to about 1 % of the total sample for all instruments and preparations. Looking at sigma coefficients ($\sqrt{\text{GoF}}$) (Table 4), analysis results from the laboratory instrument suggests a better reproducibility of the experiment using the latter. The main factor for this relies in the instrument resolution which directly influences the performed modeling for such complicated spectra, together with the added discrepancy coming from XRD and XRF mismatches using the ID2B instrument.

3.4. Crystallographic texture and structure

Carrying out geological samples XRD characterization is often a real challenge using Rietveld refinement, particularly because of the number of crystalline minerals with their own structural, microstructural and textural complexities. For instance, lizardite-1T is a layered mineral exhibiting turbostratic stacking (Brown, 1961), requiring a specific model within the Rietveld approach in order to reproduce the proper and strong asymmetry of most of the diffraction peaks. This phenomenon occurs during crystallization and can be explained by the rotation and/or translation of individual octahedra and tetrahedra layers from each other's around and/or perpendicularly to the stacking direction. Furthermore, the question of the randomness of turbostratic disorder is still under discussion (Drits and Tchoubar, 2012; Viani et al., 2002). In our case we used the Ufer model to represent this crystal stacking as well as possible, assuming a totally random turbostratic disorder with a repeatability of 20 along the c-axis (Ufer et al., 2012a; Ufer et al., 2012b; Ufer et al., 2004). In addition, a texture modelled by a gaussian standard function with $<00\ell>*$ mean directions aligned with the sample normal was used. In addition to this turbostratically disordered lizardite mineral, another strongly crystallized lizardite (lizardite-2H1) was detected and justified by the presence of narrow and slightly shifted 00ℓ and $hk0$ reflections with respect to the asymmetric peaks of lizardite-1T (Mellini, 1982). This second lizardite mineral, which would appear to be secondary due to the dissolution-precipitation of lizardite-1T, is not exhibiting any crystallographic texture.

Table 3

General information on the detected minerals used in the Rietveld refinement: mineral name, COD reference, chemical formula, crystal system and space group, and models used for line broadening and crystallographic texture.

Minerals	COD reference	Formula using XRD	Crystal system + space group	Model
Lizardite-1T	9001092	(Mg, Ni)$_3$(Si$_2$O$_5$)(OH)$_4$	Trigonal P31m	Planar defect model: Ufer single turbostratic layer Texture: standard function
Lizardite-2H1	9001091	(Mg)$_3$(Si$_2$O$_5$)(OH)$_4$	Hexagonal P6$_3$cm	Crystallite sizes and microstrains: Delft model Texture: Exponential harmonics (Lmax = 8)
Olivine	3000919	(Fe, Mg)$_2$O$_4$Si	Orthorhombic Pbnm:cab	Texture: Exponential harmonics (Lmax = 8)
Enstatite	9014117	(Ca, Mn, Mg)O3(Si,Al)	Orthorhombic Pbca	Texture: Exponential harmonics (Lmax = 8)
Chromite	1011030	(Al,Cr)$_2$NiO$_4$	Cubic Fd-3 m:1	Texture: standard function Crystallite sizes and microstrains: delft

Table 4

Refined values of the weight %, atomic site occupancies based on different tools and HI0 sample preparations and reliability factors.

Instrument		Laboratory							
Sample type		*Powder*							
Minerals		Lizardite-1T	Lizardite-2H1	Olivine		Enstatite			Nichromite
Weight (%)		28 (4)	14 (2)	42 (5)		15 (2)			1.0 (0.1)
Atoms occupancies (%)	Mg^{2+}	66 (1)		40 (1)	82 (1)	16 (3)	1.5 (0.3)		
	Ni^{2+}	34 (2)							
	Fe^{2+}			60 (1)	18 (1)				
	Ca^{2+}					2 (1)	1.7 (0.2)		
	Mn^{2+}					82 (5)	97 (1)		
	Si^{4+}							100 (1)	
	Al^{3+}								
	Cr^{3+}								100 (1)
Reliability factors		Goodness of Fit = 8.41							
		Sigma $[\sqrt{GoF}]$ = 2.90							

Instrument		ID2B							
Sample type		*Powder*							
Minerals		Lizardite-1T	Lizardite-2H1	Olivine		Enstatite			Nichromite
Weight (%)		26 (1)	15 (1)	45 (2)		13 (1)			0.82 (0.01)
Atoms occupancies (%)	Mg^{2+}	98 (1)		47 (1)	92 (1)	80 (3)	99.0 (3)		
	Ni^{2+}	2 (1)							
	Fe^{2+}			53 (1)	8 (1)				
	Ca^{2+}					16 (1)	0.8 (0.1)		
	Mn^{2+}					4 (1)	0.2 (0.1)		
	Si^{4+}							95 (2)	
	Al^{3+}							5 (1)	31 (1)
	Cr^{3+}								69 (1)
Reliability factors		Goodness of Fit = 20.43							
		Sigma $[\sqrt{GoF}]$ = 4.52							

Instrument		ID2B							
Sample type		*As-sawn sample*							
Minerals		Lizardite-1T	Lizardite-2H1	Olivine		Enstatite			Nichromite
Weight (%)		8 (1)	32 (4)	15 (2)		44 (1)			1.0 (0.1)
Atoms occupancies (%)	Mg^{2+}	99 (4)		40 (2)	82 (4)				
	Ni^{2+}	1 (0.5)							
	Fe^{2+}			60 (1)	18 (2)				
	Ca^{2+}					26 (2)	0.6 (0.5)		
	Mn^{2+}					1.0 (0.5)	1.0 (0.5)		
	Si^{4+}							95 (3)	
	Al^{3+}							5 (1)	39 (1)
	Cr^{3+}								61 (1)
Reliability factors		Goodness of Fit = 15.84							
		Sigma $[\sqrt{GoF}]$ = 3.98							

In the nomenclature for harzburgites (Streckeisen, 1976), olivine and orthopyroxene are expected to be the major minerals. By combining elemental and mineral analyses in this study, it was possible to understand the possible substitutions with Fe for Mg, and Mn and Mg for Ca within olivine and orthopyroxene, identified as enstatite, respectively. Using the MAUD software, it was possible to quantify the partial occupancy of each of these elements present on the cationic sites of both minerals. Added to this structural refinement, a crystallographic texture by a spherical harmonic model (Van Houtte, 1991) allowed to better model the intensity of some peaks of these two minerals. This texture model allowed the refinement of the orientation distribution function as a series of generalized spherical harmonics (Bunge and Esling, 1982), using a L_{max} extension of 8 (Tables 3 and 4).

Finally, elemental analysis, SEM and optical microscopic studies showed the very minor presence of Cr oxides in the sample (Table 4). Both laboratory results on powder and field instrument results on as-sawn sample exclude the presence of texture for this mineral. However, in the field powder analysis using ID2B, a $<00\ell>$-fiber texture was required, even if the small amount of this mineral in the sample does not allow a large accuracy for its determination.

3.5. Comparison of Laboratory-ID2B XRD results on powder samples

Concerning powder analysis performed on laboratory and ID2B instruments (Table 4 and Fig. 4), the same minerals have been identified in similar proportions: olivine (42 wt% for laboratory and 45 wt% for ID2B), lizardite-1T (28 wt% and 26 wt%), lizardite-2H1 (14 wt% and 15 wt%), enstatite (15 wt% and 13 wt%), and chromite (1 wt% and 0.82 wt %). The most important fact is that, as far as in-field characterization is of concern, the 4 times shorter measurements operated on the ID2B instrument result in mineral quantification coherent to the ones obtained from the reference laboratory measurement. Weight% standard deviations appear around 2 times better, in favor of the in-field instrument. This can be associated to the asymmetric measurement
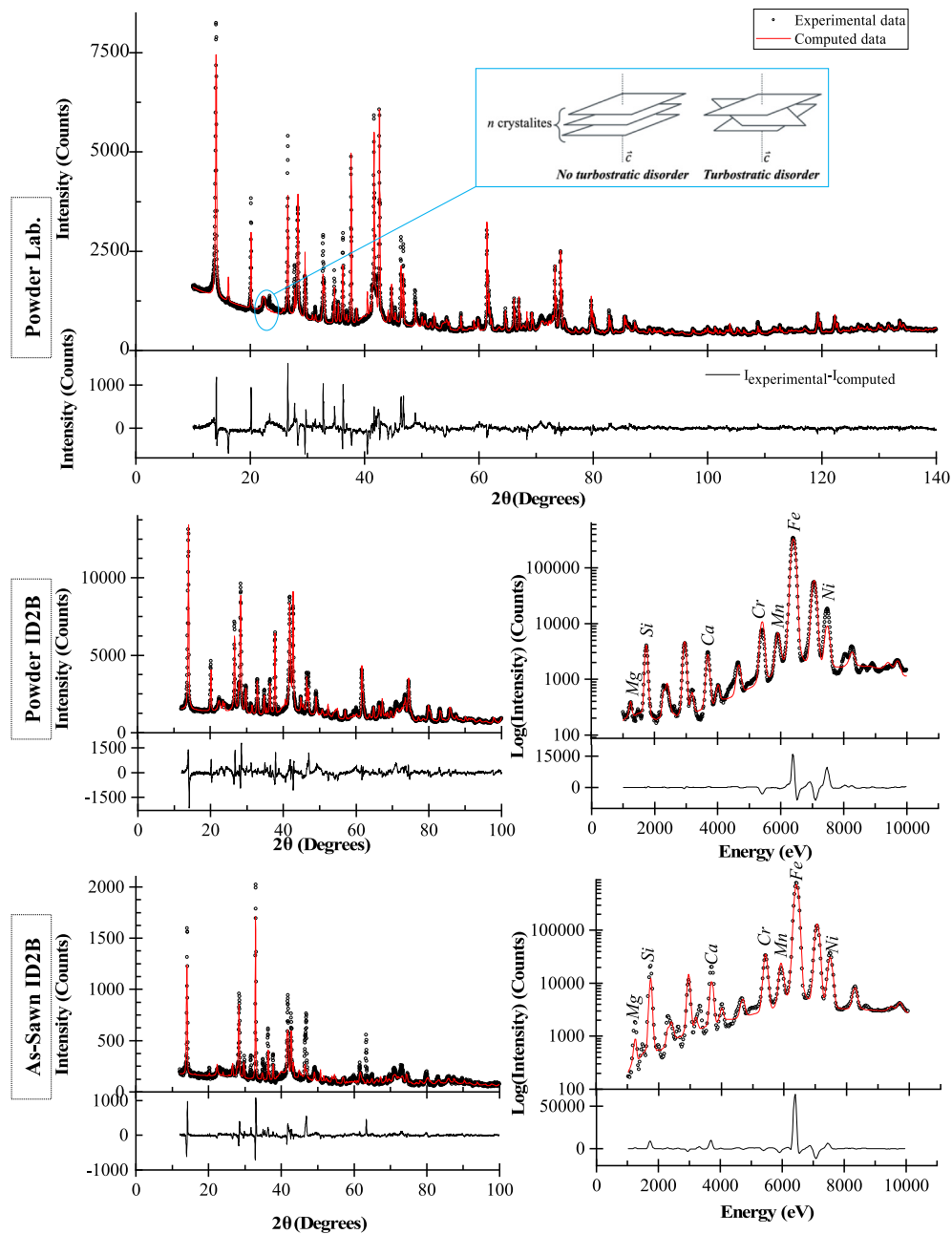
Fig. 4. (a) X-ray diffraction patterns of powder sample measured on Xpert Panalytical. (b) X-ray diffraction patterns and (c) spectrum XRF of powder sample measured on ID2B diffractometer. (d) X-ray diffraction patterns and (e) spectrum XRF of as-sawn sample measured on ID2B diffractometer. Computed patterns (red line) are surimposed to the experimental profile (coarse line). The difference curve ($I_{experimental}$-$I_{computed}$) is shown at the bottom.

configuration of ID2B which offers a better textural characterization of the textured minerals, compared to regular θ-2θ scans of laboratory instrument which only probe crystal planes that are parallel to the sample plane (i.e. with very limited texture signal).

In Table 4, the GoF is larger for the ID2B analysis. This is only due to the mismatch between XRF and XRD modeling, larger number of independent measurements being obviously harder to correctly model. Thus, for a 4-times shorter measurement, the ID2B instrument provides similar mineralogical quantification information to that obtained in the laboratory while adding within the same acquisition time the quantification of the associated chemical elements.

3.6. Comparison of results on powder and as-sawn samples

As previously stated, the main interest for measuring an as-sawn

sample is to obtain on-site real-time chemical and mineralogical information on a sample with little or no preparation. Moreover, a flat indurated as-sawn sample allows the preservation of geological structures (veins, large grains, enclave, matrix, etc.), their inter-relationships and the information derived from them.

As a preamble of such a procedure, one has to estimate how much measurements on as-sawn and powder samples can differ, and if the former can provide enough reliable analyses. Comparing the results obtained from the two types of samples, the as-sawn sample clearly exhibits large crystallite sizes for all minerals with an estimated weight percentage larger than 10 %, i.e. lizardite-2H1, olivine and enstatite. This larger crystallite size is explained by the absence of grain size reduction due to any preparation, the maximum measured crystallite size of an as-sawn sample being the largest crystallite size actually present in the specimen. In the case of chromite and 1T lizardite, the
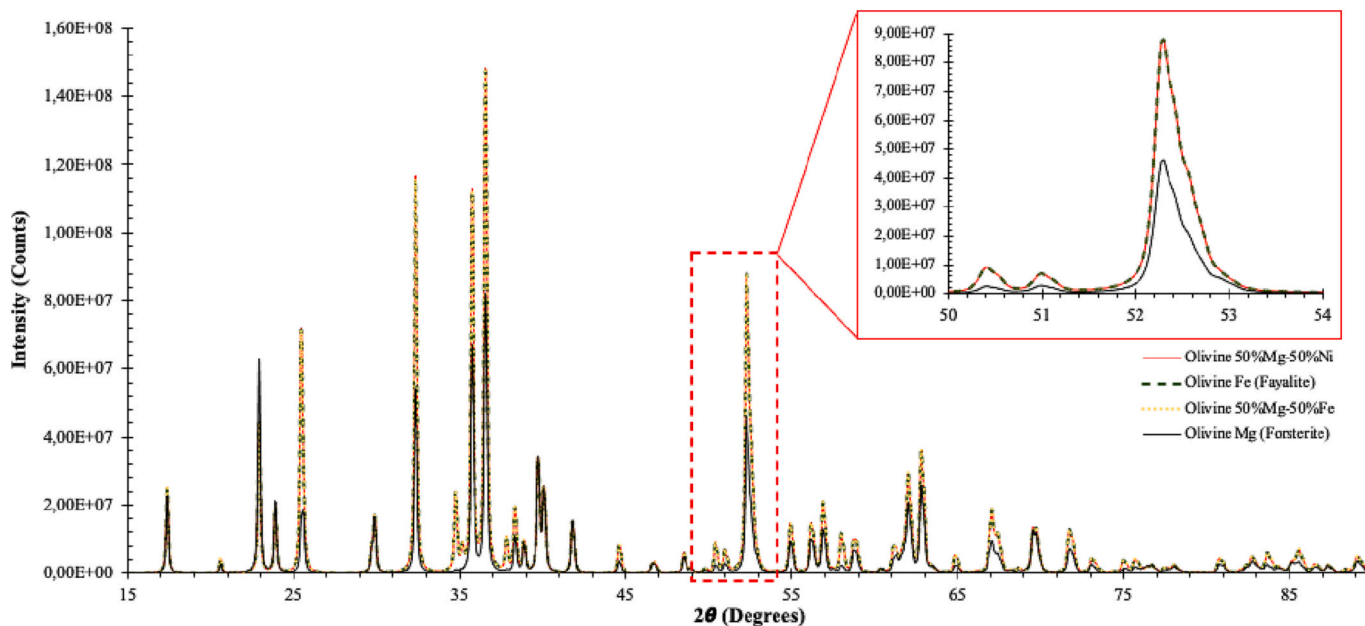
Fig. 5. Modelling of theoretical diffractograms of different solid solutions of olivine with pure magnesian pole (forsterite, black line), pure ferrous pole (fayalite, dark green dots), olivine constituted y 50% Mg - 50%Fe (yellow datted line), and olivine constituted by 50% Mg - 50% Ni (red line). (For interpretation of the references to color in this figure legend, the reader is referred to the web version of this article.)

smaller determined sizes can be explained by the low weight percentages of these minerals and their inhomogeneous distribution in the samples. Crystallite shapes and their correlated textures could also influence the results. When not ground, preferred orientations of anisotropic crystallites have to be taken into account, which can be more or less satisfactorily operated. For the raw sample (Fig. 4c), one can observe a significant deviation between experiments and fits, of the same level of magnitude as for the powder sample measured with less sensitivity to texture on the laboratory instrument (Fig. 5A). Lizardite-2H1 is overestimated with large crystallite sizes because of an insufficiently represented texture.

The weight percentage of the minerals is radically different between the powdered sample and the raw sample as-sawn, except for chromite which is explained by the sporadic character of this mineral within the sample, observed during microscopic and SEM analyses (Figs. 1 and 2). For the other minerals, the variations between the two preparations are sometimes double (31 wt% for as-sawn sample compared to the 16 wt% of the powder sample) or even triple for enstatite (from 12.6 wt% on the powder to 44 wt% on the as-sawn sample) and olivine (from 45 wt% on the powder to 12 wt% on the as-sawn sample). One of the main causes of this variation in quantification is again the difficulty of understanding the crystallographic texture in the as-sawn sample. Indeed, in an indurated sample the orientation of the crystallites is strongly constrained

and does not allow to model correctly the preferential orientation of the crystallites. The other reason for this difference in quantification is the way in which the analysis was carried out, leading to a "nugget" effect. Indeed, as illustrated on the Fig. 6, the probed area, even if continuous rotation is applied to the sample during measurements, does not cover the entire surface and therefore induces biases with regard to the size of the grains constituting the sample. Indeed, the microscopic and SEM images (Fig. 1) show a matrix of small grains composed of olivine and serpentines (lizardite-1T and lizardite-2H1) and very large grains of enstatite. As a result, the enstatite area contribution of 44 % is overestimated in the signal processing, while the olivine and the serpentines contributions areas of 55 % are underestimated. These observations obtained on the ID2B instruments respectively on the powder and the as-sawn samples show the influence of the degree of sample preparation on the mineralogical results obtained that are particularly affected by the heterogeneity of the HI0 sample visible to the naked eye (Fig. 1) as well as at micrometric scale (Fig. 2).

4. Conclusion

This study tested a new approach of combined XRF-XRD analyser that is transportable on-site and provides quantitative chemical and mineralogical analysis in real-time. Results from combined analyses on a
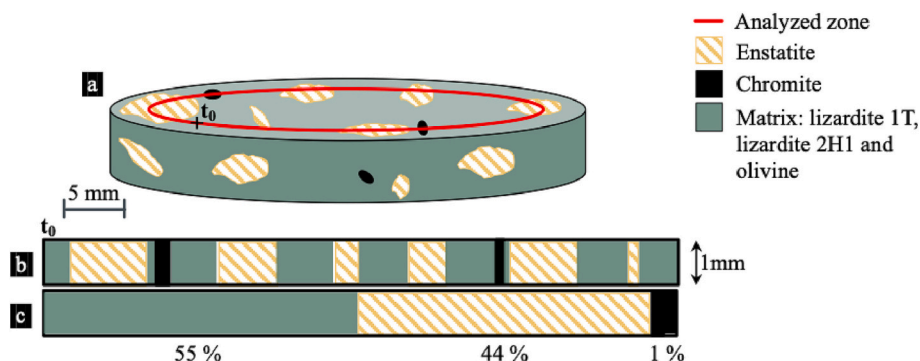
Fig. 6. Scheme showing the nugget effect during an XRD measurement on an as-sawn sample. (a) Schematic of the beam trace (red line) during XRD analysis of the as-sawn sample consisting of a matrix (lizardite 1T, lizardite 2H1 and olivine; green zone), large grains (enstatite ; yellow hatched area) and small grains (chromite ; black area). (b) Analyzed zone in XRD where t_0 is the first point analyzed and the as-sawn sample is rotated clockwise. (c) Cumulative analyzed zone in XRD. (For interpretation of the references to color in this figure legend, the reader is referred to the web version of this article.)

powder sample are in agreement with the reference analyses measured in the laboratory. Beyond the mineralogical and chemical information, the contribution of such a combined instrument also allows to refine the crystallographic texture as well as some structural disorganization (turbostratism of lizardite-1T).

The configuration of the ID2B combined instrument allows to drastically reduce the acquisition time (<30 min) with sufficiently resolved data allowing the identification and quantification of minerals down to amounts slightly lower than 1 % (chromite). The instrumental arrangement and configuration of the sample holder allows simultaneous measurement of both techniques, optimizing information and acquisition time.

Similarly, the modularity of the sample holder allows simultaneous measurements of cohesive (as-sawn) and non-cohesive (powder) samples. This approach takes into account the preparation of samples in response to the needs of a user in the field. Two options were considered and tested. The first is based on a homogenized powder sample offering better quantitative results but requiring restrictive means in the field (grinding equipment). The second option is based on the direct measurement of a heterogeneous raw sample only sawn. The advantage of this sample preparation is the one-step reduction by sawing of an indurated sample. However, this choice of preparation can lead to differences in the mineralogical quantification, especially in the presence of large grains in the beam (nugget effect). In order to minimize this nugget effect, it is possible not to rotate the sample along the phi axis but to map the sample according to x-y translations which would allow a larger surface area of the sample to be covered.

Finally, the variability in the calculated chemical proportions is attributed to the sample heterogeneity highlighted by the mineral proportions that vary slightly between powder XRD laboratory and XRD ID2B analyses, and in more pronounced for as-sawn XRD ID2B analysis.

Declaration of competing interest

The authors declare that they have no known competing financial interests or personal relationships that could have appeared to influence the work reported in this paper.

Data availability

Data will be made available on request.

Acknowledgements

References

Belsky, A., Hellenbrandt, M., Karen, V.L., Luksch, P., 2002. New developments in the Inorganic Crystal Structure Database (ICSD): accessibility in support of materials research and design. Acta Crystallographica Section B: Structural Science 58 (3), 354–369.

Bortolotti, M., Lutterotti, L., Pepponi, G., 2017. Combining XRD and XRF analysis in one Rietveld-like fitting. Powder Diffract. 32 (S1), S225–S230. https://doi.org/10.1017/S0885715617000276.

Brown, G., 1961. The X-Ray Identification and Crystal Structures of Clay Minerals. Mineralogical Society.

Bunge, H.J., Esling, C., 1982. Reproducible Textures. Textures Microstruct V 5 (N 2), 87–94. https://doi.org/10.1155/tsm.5.87.

Burkett, D.A., Graham, I.T., Ward, C.R., 2015. The application of portable X-ray diffraction to quantitative mineralogical analysis of hydrothermal systems. Can. Mineral. 53 (3), 429–454.

Drits, V.A., Tchoubar, C., 2012. X-Ray Diffraction by Disordered Lamellar Structures: Theory and Applications to Microdivided Silicates and Carbons. Springer Science & Business Media.

El Mendili, Y., Chateigner, D., Orberger, B., Gascoin, S., Bardeau, J.F., Petit, S., Dueé, C., Le Guen, M., Pilliere, H., 2019. Combined XRF, XRD, SEM-EDS, and Raman analyses on Serpentinized Harzburgite (Nickel Laterite Mine, New Caledonia): Implications for Exploration and Geometallurgy. ACS Earth and Space Chemistry 3 (10), 2237–2249. https://doi.org/10.1021/acsearthspacechem.9b00014.

Gražulis, S., Chateigner, D., Downs, R.T., Yokochi, A.F.T., Quirós, M., Lutterotti, L., Manakova, E., Butkus, J., Moeck, P., Le Bail, A., 2009. Crystallography Open Database–an open-access collection of crystal structures. J. Appl. Crystallogr. 42 (4), 726–729.

Gražulis, S., Daškevič, A., Merkys, A., Chateigner, D., Lutterotti, L., Quirós, M., Serebryanaya, N.R., Moeck, P., Downs, R.T., Le Bail, A., 2012. Crystallography Open Database (COD): an open-access collection of crystal structures and platform for world-wide collaboration. Nucleic Acids Res. 40 (D1), 420–427. https://doi.org/10.1093/nar/gkr900.

Hellenbrandt, M., 2004. The inorganic crystal structure database (ICSD) - present and future. Crystallogr. Rev. 10 (1), 17–22. https://doi.org/10.1080/08893110410001664882.

Hill, R.J., Howard, C.J., 1987. Quantitative phase analysis from neutron powder diffraction data using the Rietveld method. J. Appl. Crystallogr. 20 (6), 467–474. https://doi.org/10.1107/S0021889887086199.

Keith, J.N., Hutton, 1969. An accurate X-ray spectrographic method for the analysis of a wide range of geological samples. Geochim. Cosmochim. Acta 33 (4), 431–453.

Kimura, J., Yamada, Y., 1996. Evaluation of major and trace element XRF analyses using a flux to sample ratio of two to one glass beads. Journal of Mineralogy, Petrology and Economic Geology 91 (2), 62–72. https://doi.org/10.2465/ganko.91.62.

Lemière, B., 2018. A review of pXRF (field portable X-ray fluorescence) applications for applied geochemistry. J. Geochem. Explor. 188, 350–363. https://doi.org/10.1016/j.gexplo.2018.02.006.

Lemière, B., Uvarova, Y.A., 2020. New developments in field-portable geochemical techniques and on-site technologies and their place in mineral exploration. Geochemistry: Exploration, Environment, Analysis 20 (2), 205–216.

Lutterotti, L., Matthies, S., Wenk, H.R., 1999. MAUD: a friendly Java program for material analysis using diffraction. IUCr: Newsletter of the CPD 21 (14–15).

Lutterotti, L., Pillière, H., Fontugne, C., Boullay, P., Chateigner, D., 2019. Full-profile search–match by the Rietveld method. J. Appl. Crystallogr. 52 (3), 587–598. https://doi.org/10.1107/S160057671900342X.

Manceau, A., Calas, G., Decarreau, A., 1985. Nickel-bearing clay minerals: I. Optical spectroscopic study of nickel crystal chemistry. Clay Miner. 20 (3), 367–387. https://doi.org/10.1180/claymin.1985.020.3.08.

Maubec, N., Orberger, B., Blaineau, P.G., Villanova-de-Benavent, C., Alves, A.D.S., Duée, C., Wille, G., Delchini, S., 2021. Garnierite characterization for open mineral databases. J. Geochem. Explor. 231, 106874.

Mauger, A.J., 2007. Mapping regional alteration patterns using hyperspectral drillcore scanner. ASEG Extended Abstracts 2007 (1), 1–3. https://doi.org/10.1071/aseg2007ab086.

Mellini, M., 1982. The crystal structure of lizardite 1T: hydrogen bonds and polytypism. Am. Mineral. 67 (5–6), 587–598.

Muñoz, M., Ulrich, M., Cathelineau, M., Mathon, O., 2019. Weathering processes and crystal chemistry of Ni-bearing minerals in saprock horizons of New Caledonia ophiolite. J. Geochem. Explor. 198, 82–99.

NIST, 2015. Line position and line shape standard for powder diffraction (lanthanum hexaboride powder). In: National Institute of Standards and Technology. US Department of Commerce Gaithersburg, MD, pp. 1–5. October. https://www-s.nist.gov/srmors/certificates/660C.pdf?CFID=35608137&CFTOKEN=7e602cd95cb32152-D56C3582-CDD9-D727-1A32D16FDB2CF208.

Orloff, O., 1968. Etude Geologique et Geomorphologique des Massifs D'ultrabasites: Compris Entre Houaillou et Canala (Nouvelle-Caledonie). Université de montpellier.

Pouchou, J.L., Pichoir, F., 1984. Un nouveau modèle de calcul pour la microanalyse par spectrometrie de Rayons X partiel: Application à l'analyse d'Echantillons homogènes. La recherche aérospatiale 5, 167–191.

Sarala, P., Koskinen, H., 2018. Application of the Portable X-Ray Diffraction (pXRD) Analyser in Surficial Geological Exploration (July).

Sarrazin, P., Blake, D., Feldman, S., Chipera, S., 2005. Field deployment of a portable XRD/XRF instrument on Mars analog terrain. Adv. X-ray Anal. 48, 194–203. http://scholar.google.com/scholar?hl=en&btnG=Search&q=intitle:Field+Deployment+of+a+Portable+XRD/XRF+Instrument+on+Mars+Analog+Terrain#1.

Secchi, M., Zanatta, M., Borovin, E., Bortolotti, M., Kumar, A., Giarola, M., Sanson, A., Orberger, B., Daldosso, N., Gialanella, S., Mariotto, G., Montagna, M., Lutterotti, L., 2018. Mineralogical investigations using XRD, XRF, and Raman spectroscopy in a combined approach. J. Raman Spectrosc. 49 (6), 1023–1030. https://doi.org/10.1002/jrs.5386.

Siddiqui, M.R., Alothman, Z.A., Rahman, N., 2017. Analytical techniques in pharmaceutical analysis: a review. Arab. J. Chem. 10, S1409–S1421. https://doi.org/10.1016/j.arabjc.2013.04.016.

Streckeisen, A., 1976. To each plutonic rock its proper name. Earth Sci. Rev. 12 (1), 1–33.

Sugisaki, R., Kinoshita, T., Shimomura, T., Ando, K., 1981. An automatic X-ray fluorescence method for the trace element analyses in silicate rocks. Jour. Geol. Soc. Japan 87, 675–688.

Trotet, F., Kadar, M., Marini, D., 2015. Typology of the New Caledonian Ni-laterite deposits : from natural to industrial processes. The Society for Geology Applied to Mineral Deposits, 13th SGA meeting 3 (7), 1–4.

Ufer, K., Roth, G., Kleeberg, R., Stanjek, H., Dohrmann, R., Bergmann, J., 2004. Description of X-ray powder pattern of turbostratically disordered layer structures with a Rietveld compatible approach. Zeitschrift fur Kristallographie 219 (9), 519–527. https://doi.org/10.1524/zkri.219.9.519.44039.

Ufer, K., Kleeberg, R., Bergmann, J., Dohrmann, R., 2012a. Rietveld refinement of disordered illite-smectite mixed-layer structures by a recursive algorithm. I: One-dimensional patterns. Clay Clay Miner. 60 (5), 507–534. https://doi.org/10.1346/CCMN.2012.0600507.

Ufer, K., Kleeberg, R., Bergmann, J., Dohrmann, R., 2012b. Rietveld refinement of disordered illite-smectite mixed-layer structures by a recursive algorithm. II: Powder-pattern refinement and quantitative phase analysis. Clay Clay Miner. 60 (5), 535–552. https://doi.org/10.1346/CCMN.2012.0600508.

Ulrich, M., Picard, C., Guillot, S., Chauvel, C., Cluzel, D., Meffre, S., 2010. Multiple melting stages and refertilization as indicators for ridge to subduction formation: the New Caledonia ophiolite. Lithos 115 (1–4), 223–236.

Ulrich, M., Cathelineau, M., Muñoz, M., Boiron, M.C., Teitler, Y., Karpoff, A.M., 2019. The relative distribution of critical (Sc, REE) and transition metals (Ni, Co, Cr, Mn, V) in some Ni-laterite deposits of New Caledonia. J. Geochem. Explor. 197 (April 2018), 93–113. https://doi.org/10.1016/j.gexplo.2018.11.017.

Uvarova, Y.A., Gazley, M.F., Cleverley, J.S., Baensch, A., Lawie, D., 2016. Representative, high-spatial resolution geochemistry from diamond drill fines (powders): an example from Brukunga, Adelaide, South Australia. J. Geochem. Explor. 170, 1–9.

Uvarova, Y.A., Tassios, S., Francis, N., LeGras, M., Cleverley, J.S., Baensch, A., 2020. Top-of-holes sensing techniques: developments within Deep Exploration Technologies Cooperative Research Centre. Aust. J. Earth Sci. 1–13.

Vaitkus, A., Merkys, A., Grazulis, S., 2021. Validation of the Crystallography Open Database using the Crystallographic Information Framework. J. Appl. Crystallogr. 54, 661–672. https://doi.org/10.1107/S1600576720016532.

Van Houtte, P., 1991. A Method for the Generation of various ghost Correction Algorithms—the example of the Positivity Method and the Exponential Method. Textures and Microstructures 13 (4), 199–212. https://doi.org/10.1155/tsm.13.199.

Viani, A., Gualtieri, A.F., Artioli, G., 2002. The nature of disorder in montmorillonite by simulation of X-ray powder patterns. Am. Mineral. 87 (1), 966–975.

Wells, M.A., Ramanaidou, E.R., Quadir, M.Z., Roberts, M., Bourdet, J., Verrall, M., 2022. Morphology, composition and dissolution of chromite in the Goro lateritic nickel deposit, New Caledonia: Insight into ophiolite and laterite genesis. Ore Geol. Rev. 143, 104752.

Wicks, F., Whittaker, E.J., 1977. Serpentine textures and serpentinization. Can. Mineral. 15, 459–488.